nature catalysis

Article

https://doi.org/10.1038/s41929-024-01199-0

Long-range enhancements of micropollutant adsorption on metal-promoted photocatalysts

Received: 15 October 2023

Accepted: 26 June 2024

Published online: 19 July 2024



Photocatalysis can effectively degrade emerging (micro)pollutants in wastewater and achieve advanced water treatment objectives, wherein the low solar energy conversion efficiency remains a challenge. One key determinant is the effective adsorption of micropollutants, which is challenging to define, especially for photocatalysts with surface heterogeneity over different length scales and under (non-) reactive conditions. Here we report a generalizable imaging technique adCOMPEITS (adsorption-based competition-enabled imaging technique with super-resolution) and quantify the adsorption behaviours of non-fluorescent micropollutants on heterostructured Au/TiO₂ photocatalysts at nanometre resolution under both non-catalytic and photo(electro)catalytic conditions. We discover a long-range enhancement of micropollutant adsorption on TiO₂, which reaches micrometre-length scale and stems from the long-range surface band bending of TiO₂ upon contacting metal co-catalyst. We further engineer the band bending to effectively modulate the long-range effects on molecular adsorption. The imaging technique and the scientific discoveries here should open avenues towards understanding and engineering metal-promoted photocatalysts for many applications.

Enhancing water security is critical for global health, and it is continuously challenged by priority pollutants and emerging contaminants $^{1-3}$. Given the ever-increasing water-quality standards, conventional treatments, such as coagulation or precipitation and media filtration followed by disinfection, are becoming less effective and less economical 4,5 . Photocatalysis can effectively degrade emerging pollutants in wastewater such as trace chemicals, thus achieving more advanced water treatment objectives 6 . Among diverse photocatalysts $^{7-10}$, nanostructured TiO₂ possesses enormous attention owing to its wide

bandgap, outstanding chemical activity and stability, non-toxicity and low cost $^{7,9-11}$. Especially when a plasmonic co-catalyst such as Au is added, the resulting heterostructured Au/TiO $_2$ nanocatalysts can have enhanced performance stemming from the promoted charge separation and plasmonic effects $^{12-15}$. Currently, photocatalytic degradation of micropollutants, that is, compounds at trace concentrations below micrograms per litre in the environment, is still limited by the low overall conversion efficiency of solar energy into chemical activity 5 . One key determinant of the reaction efficiency is the effective adsorption

¹Department of Chemistry and Chemical Biology, Cornell University, Ithaca, NY, USA. ²Department of Materials Science and Engineering, National University of Singapore, Institute of Functional Intelligent Materials, and Centre for Advanced 2D Materials, National University of Singapore, Singa

of micropollutants, whose photodegradation rates on catalyst surfaces typically scale linearly with their adsorption affinity at low concentrations. However, little is known about their quantitative adsorption behaviours, especially at the nanoscale and on metal-promoted photocatalysts. Therefore, there is a pressing need for high-resolution methods capable of quantifying molecular adsorption in solution under dark and light as well as photoelectrocatalytic conditions and of differentiating adsorption across different sites on heterogeneous nanostructures.

We recently developed COMPEITS (competition-enabled imaging technique with super-resolution), which can optically image non-fluorescent processes, such as reactant surface adsorption during photocatalytic oxidation, at nanometre resolution of 16.17. COMPEITS uses a surface-catalysed fluorogenic reporter reaction for single-molecule fluorescence imaging and super-localization, followed by introducing non-fluorescent processes that compete with the reporter reaction on the catalyst surface. By quantifying the suppression of the reporter reaction, the adsorption behaviour of the competing non-fluorescent adsorbate, which could be a reactant, intermediate or product molecule, can be mapped at the nanoscale. Nevertheless, COMPEITS must be carried out under catalytic conditions owing to the requirement of a catalytic fluorogenic reaction. Catalyst–adsorbate interactions under non-reaction conditions, for example, for photocatalysts without direct charge-carrier excitation, are thus inaccessible.

Here, we report an imaging technique adCOMPEITS (adsorption-based COMPEITS), a variant of COMPEITS that can interrogate catalyst-adsorbate interactions under both reaction and non-reaction conditions. We quantify the adsorption of two representative micropollutants, pirimiphos methyl (PM, a pesticide) and diethyl phthalate (DP, a plasticizer), on individual heterostructured Au/TiO₂ photocatalysts, under dark and light as well as photoelectrocatalytic conditions. Strikingly, we discover a micrometre-range enhancement of micropollutant adsorption on TiO₂ nanorod photocatalysts, induced by the contact with Au nanoparticle co-catalysts of ~100 nm in size, in addition to a short-range adsorption enhancement at the Au-TiO₂ interface stemming from the localized surface plasmon resonance (LSPR) effect. Mechanistic investigation reveals an explicit connection of this long-range adsorption enhancement to the long-range surface band bending induced by Au/TiO₂ junction, which is generally applicable to other metal-promoted photocatalysts. This connection further enables us to manipulate the long-range adsorption enhancement via band-bending engineering, offering insights into photocatalyst design and performance optimization.

Results

Principle of adCOMPEITS

Figure 1a illustrates the principle of adCOMPEITS using surface adsorption of a fluorophore as a reporter in imaging. In a typical process, reporter fluorophores are introduced at nanomolar concentration in solution, in which their rapid diffusion smears their fluorescence signals. The adsorption of a fluorophore onto a catalyst surface pauses its motion, where its fluorescence can be imaged at the single-molecule level and its position localized at nanometre precision 12,18-20. By accumulating such localizations, the adsorption pattern on single catalyst particles can be reconstructed, as in the technique known as PAINT (points accumulation for imaging in nanoscale topography)²¹. Subsequently, the non-fluorescent molecule (or reactant) of interest is introduced to compete with the reporter fluorophore for adsorbing onto the same particle surface, leading to suppression of the reporter adsorption rate. This suppression, which informs on the adsorption of the non-fluorescent molecule, can be mapped at the same nanometre resolution. Quantitatively, the specific adsorption rate $v_R(s^{-1} \mu m^{-2})$ of the reporter (R) at any location depends on the concentrations of itself and the non-fluorescent molecule L (derivation in Supplementary Note 1 and Supplementary Equation 11):

$$v_{R} = \frac{k_{R}[M]_{T}[R]}{1 + K_{L}[L] + K_{R}[R]} \xrightarrow{[R] \to 0} \frac{k_{R}[M]_{T}[R]}{1 + K_{L}[L]},$$
(1)

when both R and L follow Langmuir adsorption. Here, $k_{\rm R}$ is the specific adsorption rate constant of the fluorophore reporter; $[{\rm M}]_{\rm T}$ is the total surface concentration of adsorption sites; and $K_{\rm R}$ and $K_{\rm L}$ are the adsorption equilibrium constants of the reporter fluorophore and non-fluorescent molecule, respectively. Moreover, $\frac{\Delta v_{\rm R}}{v_{\rm R}} (\equiv \frac{v_0 - v_{\rm R}}{v_{\rm R}})$, where v_0 is $v_{\rm R}$ at $[{\rm L}] = 0$, equals $K_{\rm L}[{\rm L}]$ (Supplementary Equation 16) and, thus, directly scales with L's adsorption affinity ($K_{\rm L}$). Compared with COMPEITS, adCOMPEITS substantially expands the scope of materials for investigation since no catalytic capability for a fluorogenic reaction is required, which also enables the investigation of molecular adsorption under non-reaction conditions for photocatalysts (more discussions on the generality and limitations are in Supplementary Note 2).

AdCOMPEITS uncovers long- and short-range adsorption enhancements

We implemented adCOMPEITS to study the adsorption of micropollutants PM and DP on Au/TiO₂ photocatalysts, prepared by depositing ~100 nm Au nanoparticles on rutile ${\rm TiO_2}$ nanorods 9,10 of ~250 nm in width and a few micrometres in length (Supplementary Fig. 1a-c) and annealing them on an indium tin oxide (ITO) substrate (Fig. 1a and Supplementary Methods). By controlling the ratio of Au nanoparticles and TiO₂ nanorods, heterostructures featuring a Au/TiO₂ pair can be formed in the products (scanning electron microscopy (SEM) images in Fig. 1d and Supplementary Fig. 3). The pesticide PM is a target pollutant for advanced water treatment: the plasticizer DP is a priority pollutant (Fig. 1a)^{1,22}. The reporter fluorophore was a Cy3.5 derivative (Supplementary Fig. 5a), excitable at 561 nm. Figure 1b shows the nanoscale mapping of reporter adsorption on a single Au/TiO₂ nanostructure, in which the Au nanoparticle sits approximately at the centre of the TiO₂ nanorod (Fig. 1d). Without any competing adsorbate, both the TiO₂ nanorod and the attached Au nanoparticle are clearly resolved. Upon introducing PM, the mapped adsorption events (n) of Cy3.5 over a same time period decreases substantially across the nanostructure, reporting their adsorption competition (Fig. 1c). Since the number of detected reporter fluorophore scales with $v_{\rm p}$, we can compute an image of $\frac{\Delta n}{\Delta t} \propto K_1$, which directly reflects the competitor binding affinity and where Δn is the difference without and with the competitor (Fig. 1e and Supplementary Equation 16). This image, termed adCOMPEITS image wherein the brighter pixels correspond to higher K_1 , immediately shows that the pesticide PM's adsorption on the Au co-catalyst is stronger than on TiO₂ within a single Au/TiO₂ heterostructured photocatalyst (Fig. 1e).

The overall spatial resolution of ~35 nm of correlated adCOMPEITS-SEM imaging allows for dissecting the TiO₂ nanorod into segments lengthwise (Fig. 1d,e and Supplementary Note 3). When [PM] is in the range of from 1 µM to 1 mM, the adCOMPEITS titration curves of the centre segment, which has the attached Au nanoparticle, and of the end TiO₂ segments are distinct (Fig. 1f), with PM's adsorption affinity at the centre being ~43% stronger and suggesting a Au-induced adsorption enhancement. This enhancement is clearer by projecting onto one dimension the adCOMPEITS image or examining the extracted adsorption equilibrium constant K of each segment along the nanorod length (Fig. 1g); both show a peak adsorption enhancement at the Au-attached segment, which decays exponentially towards the nanorod's two ends. No such adsorption enhancement was observed on isolated TiO₂ nanorods (Supplementary Fig. 10), indicating that such enhancement is exerted by the Au co-catalyst. More importantly, the exponential decay distance x_0 is ~1.2 μ m (Fig. 1g, bottom), an order of magnitude larger than the physical dimension of the Au nanoparticle, reflecting a long-range adsorption enhancement that is a remarkable observation in metal-promoted photocatalysts.

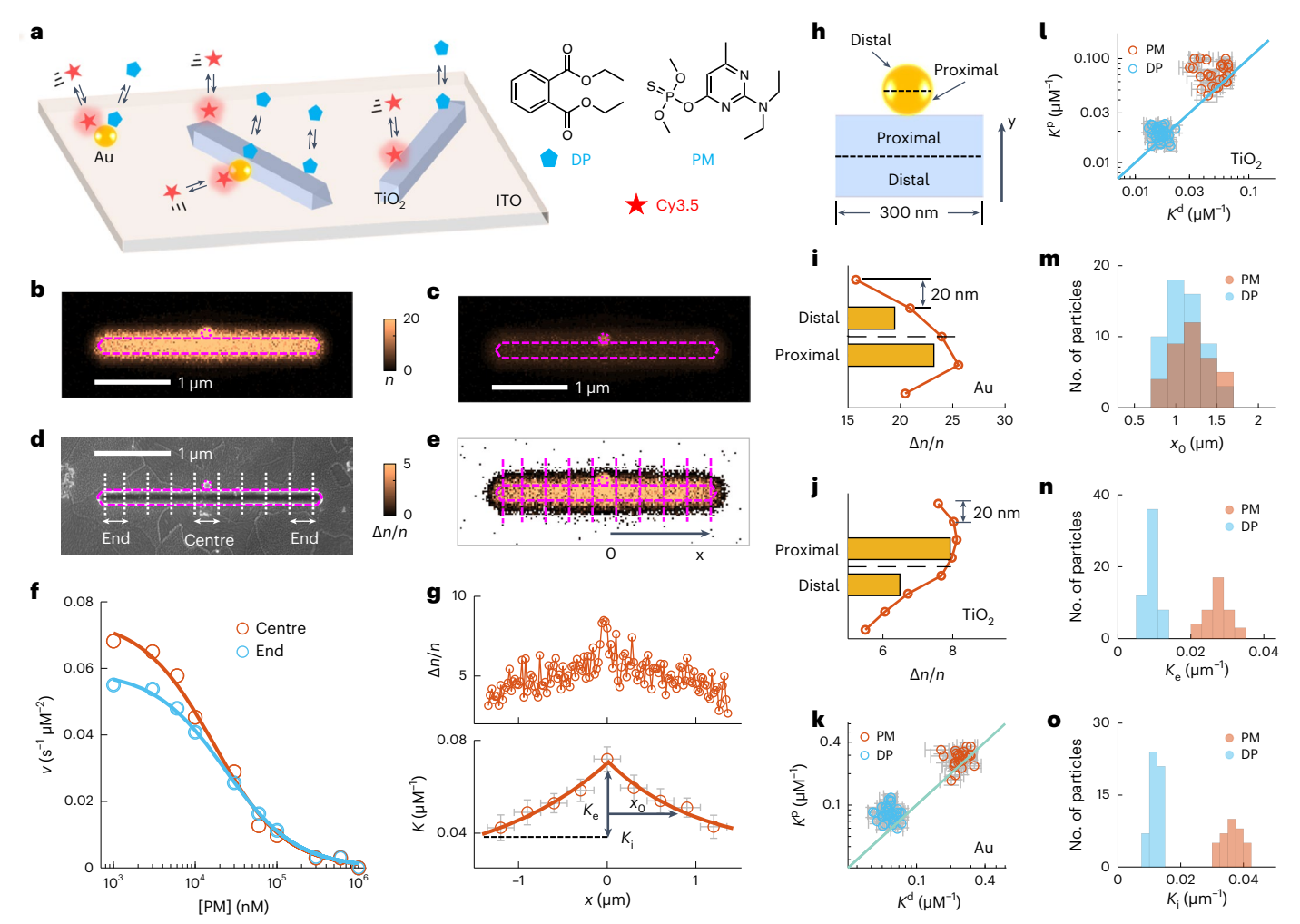


Fig. 1|**AdCOMPEITS reveals long- and short-range micropollutant adsorption enhancements. a**, Illustration of adCOMPEITS and experimental design. **b, c**, Two-dimensional histograms of single-molecule localizations of Cy3.5 adsorption on a single Au/TiO₂ at [Cy3.5] = 30 nM in the absence (**b**) and presence (**c**) of 100 μM PM. Bin size: 20^2 nm²; colour bar applies to both **b** and **c**. Scale bar in **b** applies to **b–e**. Magenta-dashed line: structural contour from SEM in **d**. **d**, SEM image of the Au/TiO₂ nanostructure in **b** and **c**. The vertical lines dissect the TiO₂ nanorods into 300 nm segments lengthwise (Supplementary Note 3). **e**, AdCOMPEITS image derived from $\Delta n/n = (n_0 - n)/n$ between **b** and **c**. **f**, AdCOMPEITS titration and fitting with equation (1) of the centre and the average of two end segments of the TiO₂ nanorod in **b–e**. **g**, One-dimensional projection of the adCOMPEITS image and the fitted *K* of individual TiO₂ segments as dissected in **d** and **e**. *x*-error bars represent the segment length; *y*-error bars are 95% confidence bound from data fitting with equation (1). Solid red

lines: bidirectional fitting with $K = K_e \exp(-|x|/x_0) + K_l$. K_e , K_i and x_0 reflect the adsorption enhancement amplitude near the Au–TiO $_2$ interface, the intrinsic adsorption equilibrium constant on the side facets of TiO $_2$ and the decay distance constant, respectively. \mathbf{h} , Scheme of dissecting the Au–TiO $_2$ interface region into proximal and distal Au and TiO $_2$ halves. \mathbf{i} , \mathbf{j} , One-dimensional projections of the adCOMPEITS image of the Au–TiO $_2$ interface region in \mathbf{e} on the y axis. The bars are the averages of data points within the proximal and distal Au (\mathbf{i}) and TiO $_2$ (\mathbf{j}) halves. The dashed lines represent the horizontal lines passing through the centroids of Au and interface TiO $_2$ segment. \mathbf{k} , \mathbf{l} , K of PM and DP on the distal (K^d) versus proximal (K^p) halves of Au (\mathbf{k}) and TiO $_2$ (\mathbf{l}) centre segment as defined in \mathbf{h} for 26 and 39 Au/TiO $_2$ nanostructures. Each point: one nanostructure. Lightgreen line: diagonal. x_iy -error bars: 95% confidence bound from data fitting with equation (1). \mathbf{m} - \mathbf{o} , Distributions of x_0 (\mathbf{m}), K_e (\mathbf{n}) and K_i (\mathbf{o}) for PM and DP adsorption among individual Au/TiO $_2$ nanostructures.

We further dissected the Au nanoparticle and the centre ${\rm TiO_2}$ segment into proximal and distal halves relative to the ${\rm Au-TiO_2}$ interface (Fig. 1h). For either the Au nanoparticle or the ${\rm TiO_2}$ centre segment, its half proximal to the interface shows stronger PM adsorption affinity than the distal half (Fig. 1i,j). In contrast, such local differences are unobserved on separate Au nanoparticles and ${\rm TiO_2}$ nanorods (Supplementary Figs. 10 and 11). Therefore, the ${\rm Au-TiO_2}$ interface also renders a short-range adsorption enhancement of the micropollutant on such metal-promoted photocatalysts.

We imaged PM and DP adsorption on many Au/TiO₂ nanostructures. For both micropollutants, such hetero-nanostructures show reproducibly stronger adsorption on the Au or TiO₂ half-segment proximal to the Au–TiO₂ interface than the distal half (Fig. 1k,l), demonstrating the generality of the short-range adsorption enhancement.

For both micropollutants, the long-range adsorption enhancement is always observed along the length of the TiO_2 nanorod in the hetero-nanostructure, with the exponential decay distance x_0 averaging at -1.3 and -1.1 µm, respectively (Fig. 1m). Moreover, the amplitude of the long-range enhancement K_e is >70% of the intrinsic adsorption affinity K_i on TiO_2 (Fig. 1g and Fig. 1n,o). Therefore, the long-range adsorption enhancement exerted by Au nanoparticle co-catalysts on TiO_2 photocatalysts is probably a universal effect, and the comparable x_0 and $K_\mathrm{e}/K_\mathrm{i}$ between the two micropollutants suggest a common underlying mechanism.

Mechanisms of adsorption enhancements

Since the long-range adsorption enhancement on TiO_2 nanorods was observed only with the Au co-catalyst, we postulated that it stems from

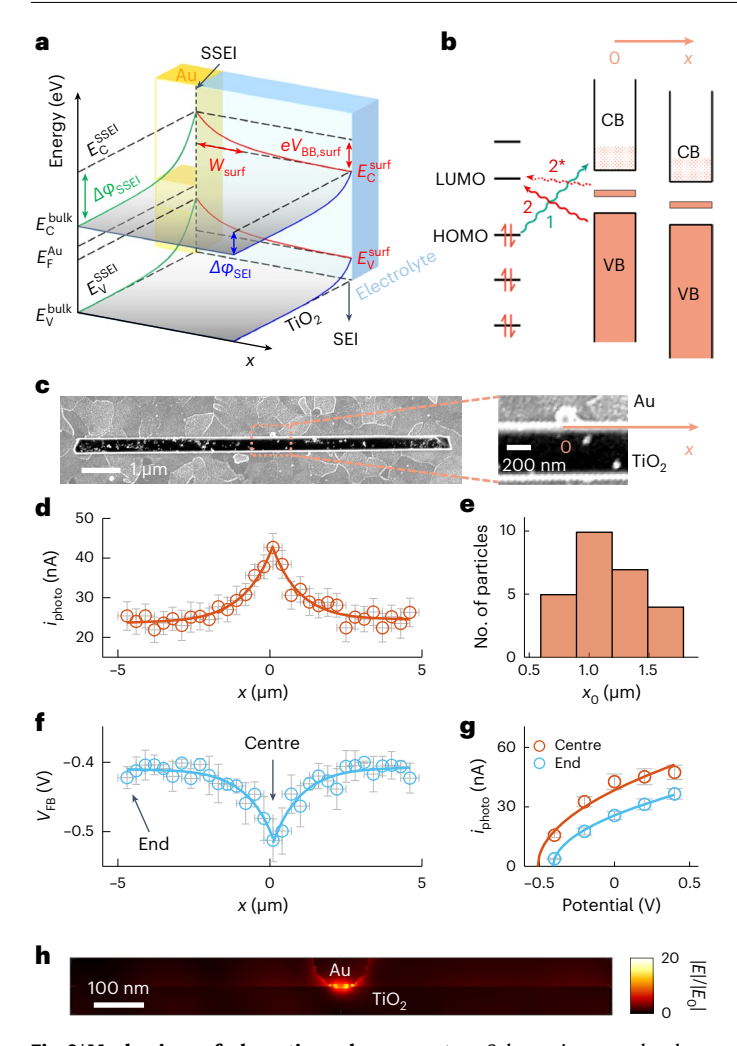


Fig. 2 | Mechanisms of adsorption enhancements. a, Schematic energy level diagram showing the surface and interior band bending in the Au/TiO₂: electrolyte system. $eV_{BB,surf}$ and W_{surf} are the surface band bending amplitude and bending zone width, respectively. $\Delta \varphi_{\text{SEI}}$ and $\Delta \varphi_{\text{SSEI}}$ are the band bendings into the interior of TiO₂ induced by SEI and SSEI interfaces, respectively. E_C and E_V are the energies of CB and VB edges, respectively. b, Schematic adsorbate-TiO₂ bonding interactions, showing the forward donation (type 1) and back donation interactions (types 2 and 2*). The shadow in CB illustrates the presence of electrons for the n-type semiconductor rutile TiO2, which also has occupied in-gap states from surface defects. c, SEM image of a Au/TiO₂ nanostructure (left) and the zoomed-in Au-TiO₂ interface region (right). **d**, Subparticle photoanodic current i_{photo} of the Au/TiO₂ nanostructure in $\bf c$ at an applied potential of 0 V versus Ag/AgCl. Solid lines: bidirectional exponential fitting. x and y errors represent the size of focused laser spot and s.d. of i_{photo} data noise, respectively (Supplementary Note 5). **e**, Distribution of the exponential distance x_0 of i_{photo} 's spatial profile from 26 Au/TiO₂ nanostructures. **f**, Subparticle V_{FB} of the Au/TiO₂ nanostructure in c. Solid lines: inverted bidirectional exponential fitting. x and y errors represent the size of focused laser spot and 95% confidence bound from data fitting, respectively. g, Comparison of the potential dependence of the measured local photocurrent at the centre and the end position of the TiO₂ nanorod marked in ${f f}$. y errors represent the s.d. of $i_{
m photo}$ data noise. ${f h}$, FDTD calculations showing the EF distribution (E) on a Au/TiO2 nanorod relative to that (E_0) of the counterpart bare TiO₂ nanorod; the Au-TiO₂ interface constitutes a EF hot spot. Here, the 561 nm laser propagation vector **k** and polarization vector **e** are in [100] and [010] directions; see Supplementary Note 6 for details.

the long-range band bending of energy levels on the surface of ${\rm TiO_2}$ upon contacting Au (Fig. 2a, red lines). Energetically, the Fermi level of rutile ${\rm TiO_2}(E_F^{\rm TiO_2})$, an n-type semiconductor 9 , is higher than that of Au $(E_F^{\rm Au})^{8,23}$, generating a downward band bending of ${\rm TiO_2}$ from the

junction, with a bending degree eV_{BB} (e is the electron charge and $eV_{BB} = E_F^{TiO_2} - E_F^{Au}$; note V_{BB} is negative) and a bending zone width W (Fig. 2a, red lines)²⁴. In bulk metal–semiconductor junctions, such band bending occurs over tens of nanometres (that is, magnitude of W) into the semiconductor interior^{25,26}. In contrast, the surface of TiO₂ where molecular adsorption occurs is two-dimensional (2D); the surface electronic states are confined to the top few atom layers; and band bending in 2D or pseudo-2D materials follows an approximate exponential decay away from the junction over micrometre scales (Fig. 2a, red lines), as shown recently both theoretically²⁷ and experimentally^{28,29}. These spatially varying surface energy levels of TiO₂ should lead to different bonding interactions with adsorbates (for example, the micropollutant PM and DP here), which should follow similar spatial patterns.

Frontier orbital interactions³⁰ play major roles in adsorbate-surface bonding. In forward donation interactions, the highest occupied molecular orbital (HOMO) of the adsorbate donates electron density to the conduction band (CB) on the surface of TiO₂ (type 1; Fig. 2b, green wiggle-arrow). In back donation interactions, the lowest unoccupied molecular orbital (LUMO) of the adsorbate accepts electron density from the valence band (VB) and the occupied in-gap states on the TiO₂ surface (types 2 and 2*, respectively; Fig. 2b, red wiggle-arrows). Closer to the Au/TiO₂ junction, the surface energy levels of TiO₂ are higher (Fig. 2a, red lines, and Fig. 2b, middle); this should lead to better orbital overlap for stronger back donations, which, if dominating PM and DP's bonding with TiO₂ surface, would rationalize their adsorption enhancement near the junction that extends over micrometres away (Fig. 1g). Consistently, for aromatic molecules such as PM and DP, their low-lying unoccupied orbitals are often involved in back donation interactions with surfaces 31,32.

Moreover, upon contacting electrolytes, the Au-induced band bending on the surface of ${\rm TiO_2}$ should give rise to a position-dependent band bending degree ($\Delta \phi_{\rm SEI}$) across the solid–electrolyte interface (SEI) perpendicular to the surface: steeper at the Au/TiO_2-electrolyte interface (solid–solid–electrolyte interface, SSEI; Fig. 2a, green lines), shallower far from the Au/TiO_2 junction (Fig. 2a, blue lines) and varying continuously along the ${\rm TiO_2}$ surface. When using such nanostructures as photoanodes, this $\Delta \phi_{\rm SEI}$ variation should give position-dependent photoelectrochemical properties on the ${\rm TiO_2}$ nanorod surface, for example, more negative flatband potentials ($V_{\rm FB}$) closer to the Au/TiO_2 junction and correspondingly larger photoanodic currents ($i_{\rm photo}$) due to more efficient charge separation 8,33 .

Therefore, to validate this TiO_2 surface band bending mechanism, we measured subparticle i_{photo} on single $\mathrm{Au/TiO}_2$ photocatalysts under photoanodic conditions via focused laser excitation in a three-electrode microfluidic photoelectrochemical cell, in which $\mathrm{SO_3}^{2-}$ and water act as hole scavengers (Methods and Supplementary Note 5)^{10,28}. Strikingly, i_{photo} is largest at the $\mathrm{Au/TiO}_2$ junction and decays exponentially away towards the two ends (Fig. 2d), as predicted from the spatial variation of $\Delta \phi_{\mathrm{SEI}}$ and following the same spatial pattern of the adsorption affinity (K) (Fig. 1g). Moreover, the exponential distance x_0 is ~1.2 ± 0.3 µm (Fig. 2d), reproducible among tens of Au/TiO2 nanostructures we measured (Fig. 2e) and the same as that of the long-range adsorption enhancement (Fig. 1g,m). As comparison, no such position-dependent i_{photo} was observed on isolated TiO2 nanorods (Supplementary Fig. 20a).

We further titrated subparticle $i_{\rm photo}$ across a range of applied potentials (Fig. 2g) and extracted the flatband potential $V_{\rm FB}$ using the Gärtner–Butler model 10,34,35 on single Au/TiO $_2$ nanostructures. As predicted, $V_{\rm FB}$ is more negative at the Au/TiO $_2$ junction and becomes less negative away from the junction, following an expected inverted exponential decay with the exponential distance $x_0 \approx 1 \, \mu m$ (Fig. 2f), in agreement with the spatial patterns of adsorption and photocurrent enhancements. Altogether, such subparticle photoelectrochemical behaviours support that the underlying mechanism of the long-range

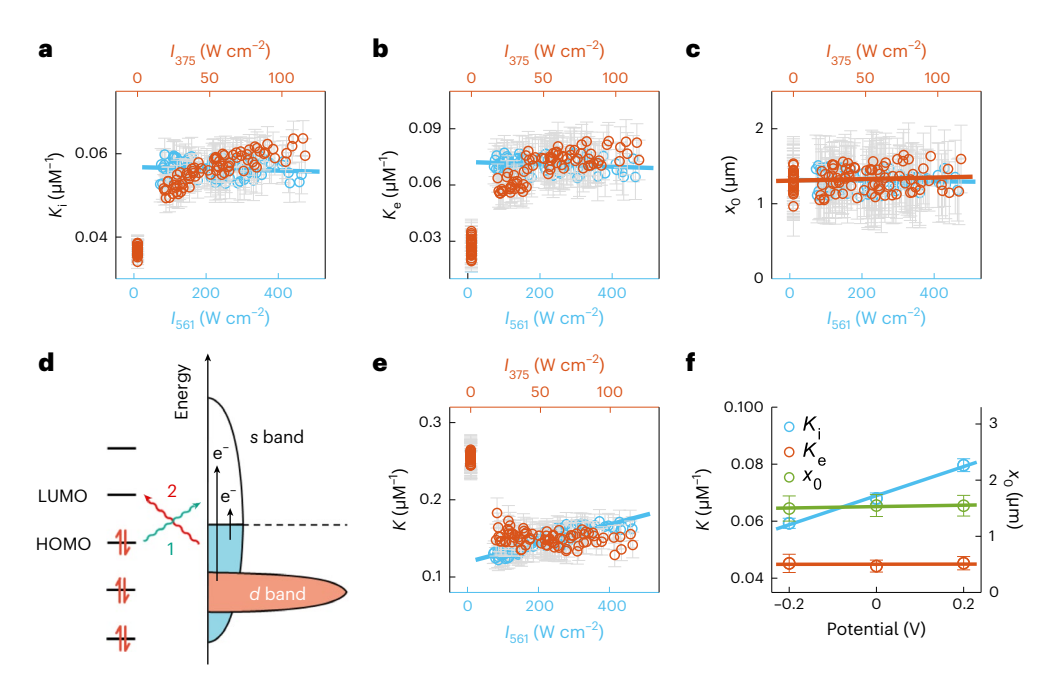


Fig. 3 | Micropollutant adsorption under photocatalytic and photoelectrocatalytic conditions. a-c, The 375 and 561 nm laser intensity I effects on PM adsorption and its long-range enhancement on TiO $_2$ of 26 Au/TiO $_2$ nanostructures: K_i (a), K_e (b) and X_0 (c). d, Schematic adsorbate—Au bonding interactions showing the forward donation (type 1) and back donation interactions (type 2). e, I_{375} - and I_{561} -dependent PM adsorption on Au of 26 Au/

 TiO_2 nanostructures. ${\bf f}$, Electrochemical potential effects on PM adsorption on TiO_2 of 26 Au/ TiO_2 nanostructures. Potentials are versus Ag/AgCl electrode. Each symbol in ${\bf a}$ – ${\bf c}$ and ${\bf e}$ represents one nanostructure. Lines in ${\bf a}$ – ${\bf c}$, ${\bf e}$ and ${\bf f}$ are linear fits. Error bars in ${\bf a}$ – ${\bf c}$ and ${\bf e}$ are 95% confidence bounds from data fitting with $K=K_{\bf e}\exp(-|x|/x_0)+K_i$ and equation (1), respectively. The error bars in ${\bf f}$ are the s.d. among single-particle values. The data in ${\bf f}$ are presented as mean values \pm s.d.

adsorption enhancement is the long-range surface band bending on ${\rm TiO_2}$ induced by contacting with Au, in which the adsorption enhancement amplitude $K_{\rm e}$ and the exponential distance constant x_0 (Fig. 1g) are proportional to the surface band bending degree $eV_{\rm BB,surf}$ and the bending zone width $W_{\rm surf}$, respectively (Fig. 2a, red lines).

Regarding the short-range adsorption enhancement at the Au–TiO $_2$ interface (Fig. 1i,j), it can be attributed to Au nanoparticle's LSPR that is excited by the 561 nm laser, which we use to induce the reporter fluorophore fluorescence. LSPR can create a strong electric field (EF) localized at the Au–TiO $_2$ interface, known to promote molecular adsorption through dipole–dipole interaction 36,37. Consistently, finite-difference time-domain (FDTD) calculations indeed show enhanced EF at the Au–TiO $_2$ interface (Fig. 2h and Supplementary Fig. 22).

Subparticle adsorption mapping under photo(electro) catalytic conditions

To probe micropollutant adsorption under photocatalytic conditions (that is, no applied potential on the ITO substrate with an open circuit), we added a 375 nm laser that excites charge carriers in TiO₂ across the bandgap and focused on PM adsorption as a representative micropollutant. Strikingly, the 375 nm laser illumination strengthens both K_i , the intrinsic adsorption equilibrium constant, and K_e, the long-range adsorption enhancement amplitude, of PM adsorption on TiO2 of Au/TiO2 nanostructures, and this strengthening is augmented with higher 375 nm laser intensities (Fig. 3a,b), which is a remarkable discovery enabled by adCOMPEITS. Under photocatalytic conditions, 375 nm laser illumination is known to generate oxygen vacancies and create occupied in-gap states in TiO₂(ref.38); these additional in-gap states should strengthen the type 2* back donation interaction between PM and TiO₂ (Fig. 2b), thus rationalizing the K_i strengthening. Consistently, PM adsorption affinity on isolated TiO₂ nanorods shows a similar 375 nm laser effect (Supplementary Fig. 23c). The creation of more in-gap states should also enlarge the adsorption strength difference between locations near the $\mathrm{Au-TiO_2}$ interface and those on the distant $\mathrm{TiO_2}$ surface, giving rise to the observed larger long-range enhancement amplitude K_e , whose main contribution is probably from back donation interactions as discussed above (Fig. 2b). For x_o , the exponential distance of long-range enhancement, no discernible change is observed (Fig. 3c), reflecting that the surface band bending zone width of $\mathrm{TiO_2}$ is barely affected by the 375 nm laser under our experimental laser intensities (< $10^3 \,\mathrm{W}$ cm⁻²).

In sharp contrast, additional 375 nm laser illumination weakened PM adsorption on Au of ${\rm Au/TiO_2}$ nanostructures: the higher the laser intensity, the smaller the adsorption equilibrium constant K (Fig. 3e). As 375 nm laser can efficiently excite d-to-s inter-band electronic transitions in Au (ref. 39), the originally unoccupied levels in Au should have increased electron population, which should weaken both the type 1 forward donation and the type 2 back donation interactions (Fig. 3d). Consistently, similar 375 nm laser-induced weakening of PM adsorption was also observed on isolated Au nanoparticles (Supplementary Fig. 23a). Expectedly, no notable change was observed in the short-range enhancement for either Au or ${\rm TiO_2}$ in the ${\rm Au/TiO_2}$ nanostructures (Supplementary Fig. 24) owing to the independence of LSPR effect of Au on the 375 nm laser.

We also varied the intensity of the 561 nm laser, which was always present for exciting the fluorophore reporter and also excites the LSPR of Au. No discernible change was observed on PM adsorption on ${\rm TiO_2}$ of ${\rm Au/TiO_2}$ nanostructures (Fig. $3{\rm a-c}$), nor on isolated ${\rm TiO_2}$ nanorods (Supplementary Fig. 23c), consistent with that ${\rm TiO_2}$ barely absorbs 561 nm light. On Au of ${\rm Au/TiO_2}$ nanostructures (Fig. 3e) and on isolated Au particles (Supplementary Fig. 23a), increasing 561 nm laser intensity expectedly strengthens PM adsorption, corroborating the role of the LSPR-induced EF effect on adsorption here. Consistently, the short-range adsorption enhancement on Au and ${\rm TiO_2}$, attributed to the same LSPR effect, is also strengthened by increasing 561 nm laser intensity (Supplementary Fig. 24).

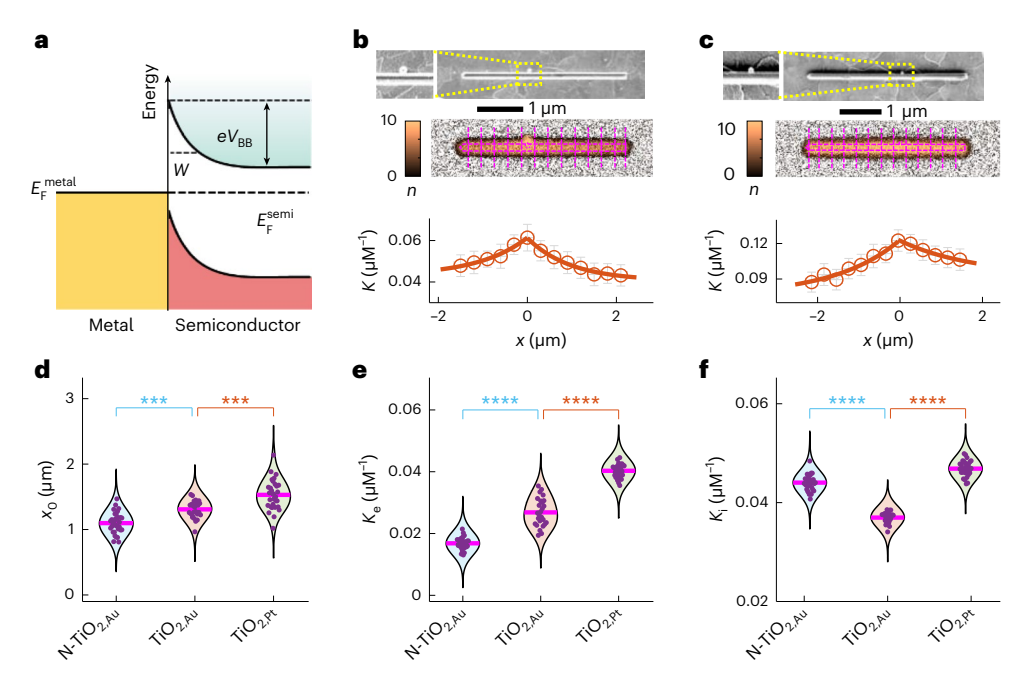


Fig. 4 | **Band bending engineering to manipulate long-range adsorption enhancement. a**, Schematic showing the band bending of semiconductor induced by metal–semiconductor contact. $eV_{\rm BB} = E_{\rm F}^{\rm semi} - E_{\rm F}^{\rm metal}$, where $E_{\rm F}^{\rm semi}$ and $E_{\rm F}^{\rm metal}$ are the Fermi levels of semiconductor and metal, respectively. **b.c.** Representative SEM and adCOMPEITS image and the fitted adsorption equilibrium constant K of PM on individual TiO₂ segments for a representative Au/N-TiO₂ (**b**) and Pt/TiO₂ nanostructure (**c**). Insets on the top left show the zoom-in of the metal–semiconductor interface areas. The magenta lines in the

middle panels show contours of metal–semiconductor nanostructure from SEM and dissection of TiO2. The error bars are 95% confidence bound from data fitting with equation (1). The scale bars in **b** and **c** also apply to the adCOMPEITS images. **d-f**, Violin plots showing the effect of N-doping of TiO2 and Pt as the co-catalyst on the long-range adsorption enhancement parameters: x_0 (**d**), K_e (**e**) and K_1 (**f**). Magenta lines: mean values. ***P < 0.001; ****P < 0.0001; two-sided t-test. The calculated P values are 1.1×10^{-4} and 7.6×10^{-4} (**d**), 7.3×10^{-11} and 6.0×10^{-13} (**e**), 1.2×10^{-14} and 9.1×10^{-19} (**f**).

We further applied electrochemical potentials (-0.2 to 0.2 V versus Ag/AgCl electrode) to examine micropollutant adsorption under photoelectrocatalytic conditions, under which there is an appreciable photoanodic current resulting from water oxidation (dominant; Fig. 2d,f)^{10,40} and PM oxidation. Interestingly, for PM adsorption on TiO₂ of Au/TiO₂ nanostructures, K_i increases with more positive potentials (Fig. 3f), attributable to electron drain in TiO₂'s CB and, thus, strengthening of the type 1 forward donation interactions (Fig. 2b). No clear trend was observed for K_e and x_0 (Fig. 3f), consistent with that the applied potential should not affect back donation interactions that involves the TiO₂'s valance band and that dominates the long-range adsorption enhancement effect.

No change was discernible for PM adsorption on Au of Au/TiO_2 with applied potentials (Supplementary Fig. 26a), suggesting that potential tuning in this range does not discernibly change the electron population of levels that are involved in the forward and back donation interactions. Consistently, no change on PM adsorption was observed at the $Au-TiO_2$ interface or on isolated Au particles with applied potentials (Supplementary Fig. 27).

Altogether, under photocatalytic and photoelectrocatalytic conditions, micropollutant adsorption on metal-promoted photocatalysts can be strongly influenced by light or electrochemical potential, in which the long- and short-range adsorption enhancements can behave differently.

Tuning long-range adsorption enhancement via band-bending engineering

As demonstrated above, the long-range adsorption enhancement of micropollutants on TiO_2 of Au/TiO_2 originates from the Au-induced surface band bending of TiO_2 . In such metal–semiconductor junctions,

the bending zone width scales with $(\frac{V_{\rm BB}}{eN_{\rm d}})^{\frac{1}{2}}$, where $N_{\rm d}$ is the density of

electron donors²³ (for example, oxygen vacancies in TiO₂) (Fig. 4a). Therefore, to tune this long-range adsorption enhancement, we engineered the band bending of TiO₂ by annealing in N₂ atmosphere to synthesize N-doped TiO₂ (that is, N-TiO₂). Such N-doping is known to increase N_d and lower TiO₂'s Fermi level by creating oxygen vacancies that appear as occupied in-gap states⁴¹⁻⁴³, which should narrow the band-bending zone width as well as decrease the band-bending degree (and, thus, the adsorption enhancement amplitude) on the Au/N-TiO₂ nanostructures. Using adCOMPEITS to map PM adsorption on the Au/N-TiO₂ nanostructures, we observed an expected peak adsorption affinity at the metal-semiconductor interface that decays exponentially away from the junction (Fig. 4b). Remarkably, both the exponential distance x_0 and the adsorption enhancement amplitude K_0 on Au/N-TiO₂ are indeed smaller than those on undoped Au/TiO₂ nanostructures (Fig. 4d,e), further corroborating the surface band bending as the underlying mechanism for the long-range adsorption enhancement. Moreover, the intrinsic adsorption affinity K_i becomes larger (Fig. 4f), attributable to that N-doping creates additional occupied in-gap states in TiO₂ and thereby enhances type 2* back donation interactions (Fig. 2b). Consistently, such increase of intrinsic adsorption affinity is also observed on isolated N-TiO₂ nanorods (Supplementary Fig. 29d). In the context of catalytic reactions, the variation in molecular adsorption affinity would strongly affect the adsorption of reactant species and desorption of products, offering an effective strategy to optimize the catalytic performance.

As an alternative strategy to modulate the band bending of TiO_2 , we replaced the Au nanoparticles by Pt nanoparticles as the co-catalyst. Since the Fermi level of Pt is lower than that of Au, the band bending degree eV_{BB} is larger at the Pt/TiO_2 junction, along with a broader bending zone. Using adCOMPEITS, we again observed the long-range adsorption enhancement of PM on Pt/TiO_2 nanostructures (Fig. 4c).

More importantly, both x_0 and K_e of Pt/TiO $_2$ are larger than those of Au/TiO $_2$ nanostructures (Fig. 4d,e), further validating the role of surface band bending in rendering the long-range adsorption enhancement. Interestingly, the presence of Pt co-catalyst also strengthens K_i (Fig. 4f). Here, compared with Au, the lower Fermi level of Pt probably promotes more electron transfer from TiO $_2$ to Pt, leading to a reduced electron density in TiO $_2$'s CB and thereby strengthening forward donation interaction (Fig. 2b). It is worth emphasizing that using a different co-catalyst to effectively alter K_i , which quantifies the semiconductor's adsorption affinity micrometres away from the metal–semiconductor interface, is another demonstration of a co-catalyst's role in exerting long-range effects on molecular adsorption on photocatalysts.

Conclusions

We have developed adCOMPEITS, a generalizable method, to image non-fluorescent processes on surfaces at super-resolution under both photo(electro)catalytic and non-catalytic conditions. By examining the adsorption of micropollutants on metal-promoted semiconductor photocatalysts, we discover a surprising micrometre-range adsorption enhancement from the metal co-catalyst-photocatalyst interface, which results from the long-range surface band bending on metalsemiconductor heterostructures. As such long-range surface band bending should apply generally to metal-promoted photocatalysts, this discovery raises additional opportunities in materials engineering of metal-promoted semiconductor photocatalysts to further enhance micropollutant adsorption for photocatalytic degradation or other surface-mediated catalytic reactions. To tune the long-range effect, metal co-catalysts with different Fermi levels and semiconductor photocatalyst doping could be used to alter band bending and the associated adsorption enhancement. Our discovery of long-range adsorption enhancement and the corresponding manipulation strategies would contribute to the development of highly efficient photocatalysts for various reactions. Especially for water decontamination where the photodegradation rate scales linearly with their adsorption affinity at low concentrations, regulating micropollutant adsorption could greatly tune the catalyst-adsorbate interaction for improving the conversion efficiency of solar energy to chemical activity.

In addition, to take advantage of the long-range adsorption enhancement, there should exist some optimal physical size of photocatalysts or optimal spatial spacing (that is, loading) of metal co-catalysts to be comparable to the width of surface band bending zone. One could also envision a variety of other potential applications, such as in surface-mediated sensing and dye-sensitized solar cells, where molecule adsorption on semiconductors is crucial. The generalizable imaging technique, the obtainable molecular insights and the general underlying mechanism presented here should open avenues for further scientific discoveries.

Methods

Syntheses of TiO₂ and N-doped TiO₂ nanorods and with metal co-catalysts

Rutile TiO_2 nanorods were synthesized using a molten salt flux method reported in literature (see more details in Supplementary Methods)°. SEM characterization shows that TiO_2 nanorods have an average length and diameter of 2.42 ± 1.36 (standard deviation, s.d.) μ m and 252 ± 74 (s.d.) nm, respectively (Supplementary Fig. 1a–c). The rutile nanorods have {100} facets along their sides and {011} facets at their two ends, as shown previously¹⁰. N-TiO₂ nanorods were prepared through a reported annealing process at 450 °C for 3 h under nitrogen flow rate of 500 cc min⁻¹ (ref. 41). The successful doping of nitrogen was confirmed by the presence of an N1s peak in the X-ray photoelectron spectroscopy spectra (Supplementary Fig. 1h versus Supplementary Fig. 1d). The 100 nm Au and 70 nm Pt nanoparticles were purchased (Supplementary Methods and Supplementary Fig. 2). The metal–semiconductor heterostructures were prepared by drop-casting 3 μ 1 of the ethanol

solution containing 100 nm Au colloidal nanoparticles (-0.3 μ g ml $^{-1}$) and TiO $_2$ nanorods (-3.33 μ g ml $^{-1}$) onto the ITO or quartz slide eight times, followed by annealing in an oven at 200 °C for 1 h.

AdCOMPEITS imaging experiments and data analysis

All single-molecule fluorescence experiments for adCOMPEITS were carried out on a home-built prism-type wide-field total internal reflection fluorescence microscope (Olympus IX71) (see more details in Supplementary Note 3). Typically, a fluorescence reporter solution without or with micropollutant molecules at designed concentrations was supplied into a flow cell at a continuous flow rate of 25 μl min $^{-1}$ driven by a syringe pump (Chemyx Incorporation). A continuous wave circularly polarized 561 nm laser beam (CrystaLaser-CL561-075-O) of ~240 mW cm $^{-2}$ was focused onto the sample (of ~100 \times 136 μm^2 in illumination area) in a flow cell to directly excite the fluorescence of the reporter fluorophore Cy3.5. The fluorescence emitted by the fluorophore reporter was collected by a 60 \times numerical aperture 1.2 water-immersion objective (UPLSAPO60XW, Olympus), filtered (HQ617m73, Chroma) and detected by a back-illuminated ANDOR iXon EMCCD camera (DU897D-CSO-#BV) operated at 30 ms frame rate.

Sulfo-cyanine3.5 alkyne (Cy3.5) was used as the main fluorophore reporter for the adCOMPEITS experiments. All single-molecule imaging experiments were carried out at room temperature in 0.1 M phosphate buffer (pH 5.62). Typically, ~50,000-101,000 frames at 30 ms per frame were collected at a fluorophore concentration of 30 nM, followed by titrating solutions with 30 nM of Cy3.5 and increasing concentrations of a micropollutant molecule. The concentrations of the micropollutant molecules ranged from micromolar to millomolar, depending on their adsorption affinity. For micropollutant adsorption under photocatalytic conditions, an additional 375 nm laser with an average power density of ~60 mW cm⁻² was introduced. The laser intensity-dependent experiments were conducted following the same protocol except varying the average laser power density from -120 to ~360 mW cm⁻² for the 561 nm laser and from ~30 to ~90 mW cm⁻² for the 375 nm laser. For micropollutant adsorption under photoelectrocatalytic conditions, potentials in the range of -0.2 to 0.2 V versus Ag/AgCl was further applied other than the 561 nm (~240 mW cm⁻²) and 375 nm lasers (\sim 60 mW cm $^{-2}$).

Information of single-molecule adsorption events was extracted from the fluorescence images in the movies using a home-written MATLAB program, subtraction iOPALM (image-based quantitative photo-activated localization microscopy^{16,44,45}; Supplementary Software 1). Briefly, each fluorescence image was first subtracted by an emission image generated by averaging its backward and forward 100 frames to remove the constant emission from Au nanoparticles and the diffuse fluorescence background from varied fluorophore concentrations. The microscope stage drift was monitored in a frame-by-frame fashion by calculating the point spread function-fitted centroid position of the stable intrinsic photoluminescence of Au nanoparticles. Afterwards, any pixel in the background-subtracted image whose intensity value was greater than the mean pixel intensity plus ~3-6 s.d. was considered as a potential candidate molecule¹⁶. Only isolated TiO₂ nanorods (or N-TiO₂ nanorods), isolated Au nanoparticles, and TiO₂ nanorods with one Au (or Pt) particle appropriately attached (confirmed by SEM imaging) were selected for further analysis. The fluorescence images were further correlated with ex situ SEM imaging on the same sample after the fluorescence imaging (see details in Supplementary Note 3).

Photoelectrochemical measurements

The subnanorod photocurrent measurements were carried out in a sodium borate buffer (0.1 M, pH 8.3) mixed with Na₂SO₄ (1 M) as the supporting electrolyte and Na₂SO₃ (0.2 M) as a scavenger for the photogenerated holes in TiO₂, using a three-electrode photoelectrochemical flow cell as we previously reported 10,40 (see also Supplementary

Note 5). Typically, a focused 375 nm laser, which can effectively excite charge carriers in TiO₂ (ref. 46), was used to excite individual spots on individual nanorods in a front-side illumination geometry through the electrolyte for three consecutive 10 s on and 10 s off cycles, with an applied potential of 0.4 V versus Ag/AgCl. The diameter of the focused laser spot is ~398 nm (that is, full width at half maximum), with a maximal power density of 8.1 MW cm⁻² (Supplementary Fig. 18a,b). This spatially localized charge carrier excitation ensured that the photocurrent response originated from a local region within an individual nanorod. Electrochemical currents were collected at 0.02 s time resolution over 60 s time window. To extract the steady-state photocurrent, the measured on-off *i-t* curve (Supplementary Fig. 18c) was first subtracted by background, which was extracted via exponentially fitting the data points of laser-on segments. Afterwards, the background-subtracted i-t curve (Supplementary Fig. 18d) was smoothened using a built-in smooth function and a span of 5 via MATLAB (Supplementary Fig. 18e). To avoid the effect of laser on-off switch on the photocurrent, only the last 70% of data points of the third on and off segments were used for deriving the steady-state photocurrent (Supplementary Fig. 18f), in which the errors are the s.d. of selected data points. The subnanorod flatband potential V_{FB} was determined on the basis of the measurements of photocurrent as a function of applied potential¹⁰. The applied potential V ranged from -0.4 to 0.4 V versus Ag/AgCl, with an interval of 0.2 V.

FDTD simulations

We used the boundary element method based on the MNPBEM toolkit^{47,48} to model the EF distributions of a Au nanoparticle sitting beside a TiO₂ nanorod (Supplementary Note 6). We modelled the Au nanoparticle as a 100-nm-diameter sphere and modelled the TiO₂ nanorod as a 100 nm × 100 nm × 1,000 nm cuboid (Supplementary Fig. 22a). The xy plane is defined as parallel to the surface where both Au nanoparticle and TiO_2 nanorod sit. The Au nanosphere is in contact with the TiO₂ surface, and the spherical contact area has a radius of 10 nm (Supplementary Fig. 22b,c). The sizes of all dissected segments are <10 nm. Specifically, the segment size at the Au-TiO₂ interface is 0.1 nm, which is gradually increased for distal Au and TiO₂ segments. As our imaging experiments were done via total internal reflection excitation of the 561 nm laser, in which an evanescent wave at the ITO substrate/solution interface (that is, parallel to the xy plane) provides the excitation, the excitation light propagation is in the xy plane. We also used circular polarized 561 nm light. Therefore, to cover all the possible orientations of Au/TiO₂ heterostructure (in the xy plane) and the propagation and polarizations directions, two perpendicular propagation (along x or y, that is, [100] and [010] direction) and polarizations directions (parallel or perpendicular to the xy plane) were evaluated, giving rise to a total of four types of combination (Supplementary Fig. 22d-g). We used the dielectric permittivity data of Johnson and Christy for Au (ref. 49) and that of Wypych for TiO₂ (ref. 50). We calculated the EF intensity on a rectangular grid on the plane right above the substrate (on z = 0 nm plane).

Data availability

Raw data supporting the findings of this study are available from the authors upon reasonable request. Source data are provided with this paper.

Code availability

MATLAB codes are provided as Supplementary Software 1.

References

 Alvarez, P. J. J., Chan, C. K., Elimelech, M., Halas, N. J. & Villagran, D. Emerging opportunities for nanotechnology to enhance water security. *Nat. Nanotechnol.* 13, 634–641 (2018).

- Clara, M. et al. Removal of selected pharmaceuticals, fragrances and endocrine disrupting compounds in a membrane bioreactor and conventional wastewater treatment plants. Water Res. 39, 4797–4807 (2005).
- 3. Kim, M.-K. & Zoh, K.-D. Occurrence and removals of micropollutants in water environment. *Environ. Eng. Res.* **21**, 319–332 (2016).
- Mauter, M. S. et al. The role of nanotechnology in tackling global water challenges. *Nat. Sustain.* 1, 166–175 (2018).
- Hodges, B. C., Cates, E. L. & Kim, J.-H. Challenges and prospects of advanced oxidation water treatment processes using catalytic nanomaterials. *Nat. Nanotechnol.* 13, 642–650 (2018).
- Lotfi, S., Fischer, K., Schulze, A. & Schäfer, A. I. Photocatalytic degradation of steroid hormone micropollutants by TiO₂-coated polyethersulfone membranes in a continuous flow-through process. *Nat. Nanotechnol.* 17, 417–423 (2022).
- Chen, R. et al. Spatiotemporal imaging of charge transfer in photocatalyst particles. *Nature* 610, 296–301 (2022).
- 8. Laskowski, F. A. L. et al. Nanoscale semiconductor/catalyst interfaces in photoelectrochemistry. *Nat. Mater.* **19**, 69–76 (2020).
- 9. Liu, B. et al. Large-scale synthesis of transition-metal-doped TiO_2 nanowires with controllable overpotential. *J. Am. Chem. Soc.* **135**, 9995–9998 (2013).
- Sambur, J. B. et al. Sub-particle reaction and photocurrent mapping to optimize catalyst-modified photoanodes. *Nature* 530, 77–80 (2016).
- Schneider, J. et al. Understanding TiO₂ photocatalysis: mechanisms and materials. Chem. Rev. 114, 9919–9986 (2014).
- Zhang, Z. et al. Interfacial oxygen vacancies yielding long-lived holes in hematite mesocrystal-based photoanodes. *Nat. Commun.* 10, 4832 (2019).
- 13. Tan, S. et al. Plasmonic coupling at a metal/semiconductor interface. *Nat. Photon.* **11**, 806–812 (2017).
- Hong, J. W., Wi, D. H., Lee, S.-U. & Han, S. W. Metal-semiconductor heteronanocrystals with desired configurations for plasmonic photocatalysis. J. Am. Chem. Soc. 138, 15766–15773 (2016).
- Wang, M., Ye, M., Iocozzia, J., Lin, C. & Lin, Z. Plasmon-mediated solar energy conversion via photocatalysis in noble metal/ semiconductor composites. *Adv. Sci.* 3, 1600024 (2016).
- Mao, X., Liu, C., Hesari, M., Zou, N. & Chen, P. Super-resolution imaging of non-fluorescent reactions via competition. *Nat. Chem.* 11, 687–694 (2019).
- Ye, R. et al. Nanoscale cooperative adsorption for materials control. Nat. Commun. 12, 4287 (2021).
- Dong, B. et al. In situ quantitative single-molecule study of dynamic catalytic processes in nanoconfinement. *Nat. Catal.* 1, 135–140 (2018).
- Roeffaers, M. B. et al. Spatially resolved observation of crystal-face-dependent catalysis by single turnover counting. *Nature* 439, 572–575 (2006).
- Roeffaers, M. B. et al. Super-resolution reactivity mapping of nanostructured catalyst particles. *Angew. Chem. Int. Ed.* 48, 9285–9289 (2009).
- Sharonov, A. & Hochstrasser, R. M. Wide-field subdiffraction imaging by accumulated binding of diffusing probes. *Proc. Natl Acad. Sci. USA* 103, 18911–18916 (2006).
- Keith, L. & Telliard, W. ES&T special report: priority pollutants: I-a perspective view. Environ. Sci. Technol. 13, 416–423 (1979).
- Zhang, Z. & Yates, J. T. Jr Band bending in semiconductors: chemical and physical consequences at surfaces and interfaces. *Chem. Rev.* 112, 5520–5551 (2012).
- Brillson, L. J. Surfaces and interfaces of zinc oxide. In Semiconductors and Semimetals (eds. Svensson, B. G., Pearton, S. J. & Jagadish, C.) 105–157 (Elsevier, 2013).
- 25. Broadway, D. A. et al. Spatial mapping of band bending in semiconductor devices using in situ quantum sensors. *Nat. Electron.* **1**, 502–507 (2018).

- Butler, C. J. et al. Mapping polarization induced surface band bending on the Rashba semiconductor BiTel. Nat. Commun. 5, 4066 (2014).
- Nipane, A., Jayanti, S., Borah, A. & Teherani, J. T. Electrostatics of lateral p-n junctions in atomically thin materials. *J. Appl. Phys.* 122, 194501 (2017).
- 28. Mao, X. & Chen, P. Inter-facet junction effects on particulate photoelectrodes. *Nat. Mater.* **21**, 331–337 (2022).
- Zheng, C. et al. Direct observation of 2D electrostatics and ohmic contacts in template-grown graphene/WS₂ heterostructures. ACS Nano 11, 2785–2793 (2017).
- Hoffmann, R. A chemical and theoretical way to look at bonding on surfaces. Rev. Mod. Phys. 60, 601–628 (1988).
- 31. Hu, K. et al. Kinetic pathway for interfacial electron transfer from a semiconductor to a molecule. *Nat. Chem.* **8**, 853–859 (2016).
- Chen, G. et al. Bimetallic effect of single nanocatalysts visualized by super-resolution catalysis imaging. ACS Cent. Sci. 3, 1189–1197 (2017).
- 33. Chen, S., Takata, T. & Domen, K. Particulate photocatalysts for overall water splitting. *Nat. Rev. Mater.* **2**, 17050 (2017).
- 34. Gärtner, W. W. Depletion-layer photoeffects in semiconductors. *Phys. Rev.* **116**, 84 (1959).
- Butler, M. Photoelectrolysis and physical properties of the semiconducting electrode WO₂. J. Appl. Phys. 48, 1914–1920 (1977).
- Zhao, J. et al. Interaction of plasmon and molecular resonances for rhodamine 6G adsorbed on silver nanoparticles. *J. Am. Chem.* Soc. 129, 7647–7656 (2007).
- Zhan, C. et al. From plasmon-enhanced molecular spectroscopy to plasmon-mediated chemical reactions. *Nat. Rev. Chem.* 2, 216–230 (2018).
- Li, Y. et al. Defective TiO₂ with high photoconductive gain for efficient and stable planar heterojunction perovskite solar cells. Nat. Commun. 7, 12446 (2016).
- 39. Aslam, U., Rao, V. G., Chavez, S. & Linic, S. Catalytic conversion of solar to chemical energy on plasmonic metal nanostructures. *Nat. Catal.* **1**, 656–665 (2018).
- Hesari, M., Sambur, J. B., Mao, X., Jung, W. & Chen, P. Quantifying photocurrent loss of a single particle-particle interface in nanostructured photoelectrodes. *Nano Lett.* 19, 958–962 (2019).
- Wang, K. et al. Correlation between the H₂ response and its oxidation over TiO₂ and N doped TiO₂ under UV irradiation induced by Fermi level. Appl. Catal. B 250, 89–98 (2019).
- Hamamoto, N. et al. Effect of oxygen vacancies on adsorption of small molecules on anatase and rutile TiO₂ surfaces: a frontier orbital approach. J. Phys. Chem. C 125, 3827–3844 (2021).
- Quesada-Cabrera, R., Sotelo-Vazquez, C., Darr, J. A. & Parkin, I. P. Critical influence of surface nitrogen species on the activity of N-doped TiO₂ thin-films during photodegradation of stearic acid under UV light irradiation. Appl. Catal. B 160-161, 582-588 (2014).
- Chen, T.-Y. et al. Concentration- and chromosome-organization-dependent regulator unbinding from DNA for transcription regulation in living cells. *Nat. Commun.* 6, 7445 (2015).
- Chen, P. & Chen, T.-Y. MATLAB code package: iQPALM (image-based quantitative photo-activated localization microscopy). figshare https://doi.org/10.6084/ m9.figshare.12642617.v1 (2020).
- Ben-Shahar, Y. et al. Optimal metal domain size for photocatalysis with hybrid semiconductor-metal nanorods. *Nat. Commun.* 7, 10413 (2016).
- Waxenegger, J., Trügler, A. & Hohenester, U. Plasmonics simulations with the MNPBEM toolbox: consideration of substrates and layer structures. *Comput. Phys. Commun.* 193, 138–150 (2015).

- Hohenester, U. & Trügler, A. MNPBEM—a Matlab toolbox for the simulation of plasmonic nanoparticles. *Comput. Phys. Commun.* 183, 370–381 (2012).
- 49. Johnson, P. B. & Christy, R. W. Optical constants of the noble metals. *Phys. Rev. B* **6**, 4370–4379 (1972).
- 50. Wypych, A. et al. Dielectric properties and characterisation of titanium dioxide obtained by different chemistry methods. *J. Nanomater.* **2014**, 1–9 (2014).

Acknowledgements

The research on semiconductor photo(electro)catalysis is supported by the US Department of Energy, Office of Science, Basic Energy Sciences, Catalysis Science Program (grant no. DE-SC0004911; P.C.). The research on super-resolution imaging of metal nanoparticles is supported by the Army Research Office (grant no. W911NF-23-1-0105). The research used Cornell Center for Materials Research Shared Facilities supported by NSF (grant no. DMR-1719875). M.Z. acknowledges the support from the National University of Singapore start-up grant, National Research Foundation Singapore (grant no. U2311D4005), Centre for Hydrogen Innovations (grant no. CHI-P2023-04) and Ministry of Education (grant no. 23-0646-A0001).

Author contributions

M.Z. designed and performed experiments, synthesized particles, derived kinetic models, wrote computer codes and analysed data. W.L. contributed to adCOMPEITS method development. M.Y. performed FDTD calculations and analysis. Z.Z. contributed to photocurrent measurements. R.Y., X.M. and P.P. contributed to imaging experiments. M.Z. and P.C. analysed results and wrote the manuscript. P.C. directed research. All authors contributed to discussions.

Competing interests

P.C. and X.M. previously filed a US patent application 'Super-resolution optical imaging of non-fluorescent species' (no. 16/584,219) that is pending and encompasses the adCOMPEITS method.

Additional information

Supplementary information The online version contains supplementary material available at https://doi.org/10.1038/s41929-024-01199-0.

Correspondence and requests for materials should be addressed to Peng Chen.

Peer review information *Nature Catalysis* thanks Johan Hofkens, Dechen Jiang and Bert M. Weckhuysen for their contribution to the peer review of this work.

Reprints and permissions information is available at www.nature.com/reprints.

Publisher's note Springer Nature remains neutral with regard to jurisdictional claims in published maps and institutional affiliations.

Springer Nature or its licensor (e.g. a society or other partner) holds exclusive rights to this article under a publishing agreement with the author(s) or other rightsholder(s); author self-archiving of the accepted manuscript version of this article is solely governed by the terms of such publishing agreement and applicable law.

© The Author(s), under exclusive licence to Springer Nature Limited 2024